nature materials

ARTICLES

https://doi.org/10.1038/s41563-022-01291-5

Check for updates

Composition and phase engineering of metal chalcogenides and phosphorous chalcogenides

Jiadong Zhou[1,2,23]✉, Chao Zhu[3,4,23], Yao Zhou[5,23], Jichen Dong[6,7], Peiling Li[8], Zhaowei Zhang[9], Zhen Wang[10], Yung-Chang Lin[11], Jia Shi[12], Runwu Zhang[1], Yanzhen Zheng[13], Huimei Yu[14], Bijun Tang[3], Fucai Liu[15], Lin Wang[16], Liwei Liu[17], Gui-Bin Liu[1], Weida Hu[10], Yanfeng Gao[18], Haitao Yang[8], Weibo Gao[9], Li Lu[8,22], Yeliang Wang[17]✉, Kazu Suenaga[11], Guangtong Liu[8,22], Feng Ding[6,19], Yugui Yao[1]✉ and Zheng Liu[3,20,21]✉

Two-dimensional (2D) materials with multiphase, multielement crystals such as transition metal chalcogenides (TMCs) (based on V, Cr, Mn, Fe, Cd, Pt and Pd) and transition metal phosphorous chalcogenides (TMPCs) offer a unique platform to explore novel physical phenomena. However, the synthesis of a single-phase/single-composition crystal of these 2D materials via chemical vapour deposition is still challenging. Here we unravel a competitive-chemical-reaction-based growth mechanism to manipulate the nucleation and growth rate. Based on the growth mechanism, 67 types of TMCs and TMPCs with a defined phase, controllable structure and tunable component can be realized. The ferromagnetism and superconductivity in FeX_y can be tuned by the *y* value, such as superconductivity observed in FeX and ferromagnetism in FeS_2 monolayers, demonstrating the high quality of as-grown 2D materials. This work paves the way for the multidisciplinary exploration of 2D TMPCs and TMCs with unique properties.

Two-dimensional (2D) materials including different systems such as single (elementary), binary and ternary crystals have drawn extensive attention as they possess fundamentally physical phenomena with potential applications in quantum devices and information technology[1,2]. To study the underlying physics and realize potential applications, many efforts have been devoted to synthesize ultrathin 2D materials. To date, different bottom-up methods have been exploited for achieving different types of 2D material[3–5]. Recently, although few works have attempted to synthesize binary transition metal chalcogenides (TMCs)[6–9], the controllable synthesis of 2D binary chalcogenides with different phases/compositions remains challenging, especially for the preparation of 2D transition metal phosphorous chalcogenide (TMPC) crystals[6,10–13]. So far, no general method can be used to synthesize these 2D multiphase/multicomposition materials. This is attributed to the fact that they have variable valence states, polymorph characteristics and phases, such as MX (hexagonal and tetragonal), MX_2 (hexagonal and tetragonal), M_2X_3, M_3X_4, M_5X_8, MPX, MPX_3 and so on[14,15]. All these make the chemical reactions for preparing a single phase of TMPCs and TMCs uncontrollable. It is worth noting that these TMPCs and TMCs exhibit rich atomic structures and exotic physical properties. For example, MPX_3, Fe_xGeTe_2 and $FeSe_xTe_{1-x}$ are excellent candidates to study 2D antiferromagnetism, ferromagnetism and topological superconductivity[16–19]. Meanwhile, TMPCs provide fantastic systems to study many-body excitons and spintronic devices[20]. Therefore, the controllable synthesis of a single-phase/single-composition crystal is urgently required.

[1]Centre for Quantum Physics, Key Laboratory of Advanced Optoelectronic Quantum Architecture and Measurement (MOE), School of Physics, Beijing Institute of Technology, Beijing, China. [2]Chongqing Center for Microelectronics and Microsystems, Beijing Institute of Technology, Chongqing, People's Republic of China. [3]School of Materials Science and Engineering, Nanyang Technological University, Singapore, Singapore. [4]SEU-FEI Nano-Pico Center, Key Laboratory of MEMS of Ministry of Education, Collaborative Innovation Center for Micro/Nano Fabrication, Device and System, Southeast University, Nanjing, People's Republic of China. [5]Advanced Research Institute of Multidisciplinary Science, and School of Chemistry and Chemical Engineering, Beijing Institute of Technology, Beijing, People's Republic of China. [6]Center for Multidimensional Carbon Materials, Institute for Basic Science (IBS), Ulsan, Republic of Korea. [7]Beijing National Laboratory for Molecular Sciences, Key Laboratory of Organic Solids, Institute of Chemistry, Chinese Academy of Sciences, Beijing, People's Republic of China. [8]Beijing National Laboratory for Condensed Matter Physics, Institute of Physics, Chinese Academy of Sciences, Beijing, People's Republic of China. [9]School of Physical and Mathematical Science, Nanyang Technological University, Singapore, Singapore. [10]State Key Laboratory of Infrared Physics, Shanghai Institute of Technical Physics, Chinese Academy of Sciences, Shanghai, People's Republic of China. [11]The Institute of Scientific and Industrial Research, Osaka University, Osaka, Japan. [12]Department of Chemistry, National University of Singapore, Singapore, Singapore. [13]Beijing Key Laboratory of Green Recovery and Extraction of Rare and Precious Metals, University of Science and Technology Beijing, Beijing, People's Republic of China. [14]School of Materials Science and Engineering, East China University of Science and Technology, Shanghai, People's Republic of China. [15]School of Optoelectronic Science and Engineering, University of Electronic Science and Technology of China, Chengdu, People's Republic of China. [16]Key Laboratory of Flexible Electronics (KLOFE) & Institute of Advanced Materials (IAM), Jiangsu National Synergetic Innovation Center for Advanced Materials (SICAM), Nanjing Tech University (NanjingTech), Nanjing, People's Republic of China. [17]School of Integrated Circuits and Electronics, Beijing Institute of Technology, Beijing, People's Republic of China. [18]School of Materials Science and Engineering, Shanghai University, Shanghai, People's Republic of China. [19]School of Materials Science and Engineering, Ulsan National Institute of Science and Technology, Ulsan, Korea. [20]CINTRA CNRS/NTU/THALES, Research Techno Plaza, Singapore, Singapore. [21]School of Electrical and Electronic Engineering, Nanyang Technological University, Singapore, Singapore. [22]Present address: Songshan Lake Materials Laboratory, Guangdong, China. [23]These authors contributed equally: Jiadong Zhou, Chao Zhu, Yao Zhou. ✉e-mail: jdzhou@bit.edu.cn; yeliang.wang@bit.edu.cn; ygyao@bit.edu.cn; z.liu@ntu.edu.sg

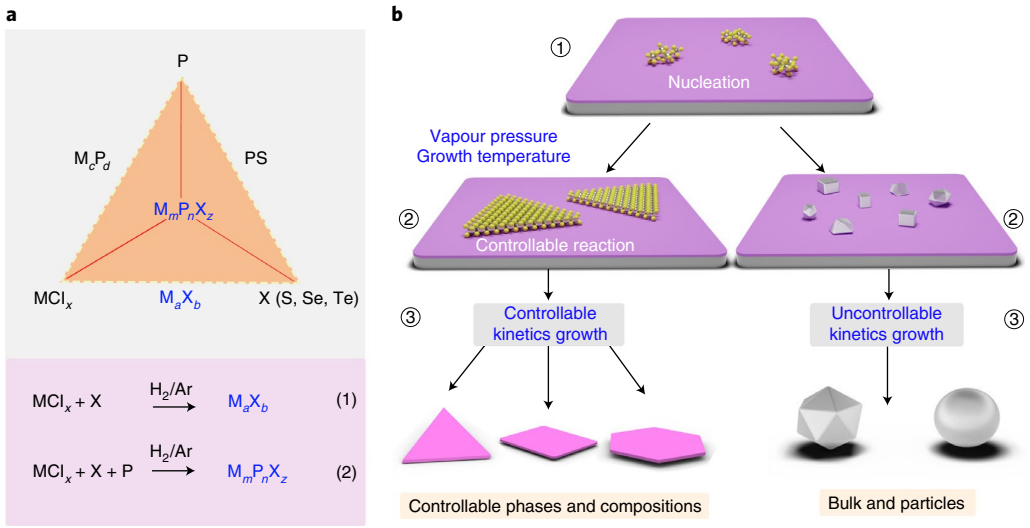

Fig. 1 | Kinetic growth mode for the controllable synthesis of M_aX_b and $M_mP_nX_z$ with different phases and compositions. a, Growth phase diagram of M_aX_b and $M_mP_nX_z$. There are different compositions such as MX, M_2X_3, M_3X_4, MX_2, M_5X_8 and MPX, MPX_3, and so on in binary M_aX_b and ternary $M_mP_nX_z$. The growth process of $M_mP_nX_z$ may involve the formation of binary crystals such as M_cP_d, PS and M_aX_b. Therefore, how to control the chemical reactions for single-phase growth is the key to realize the preparation of M_aX_b and $M_mP_nX_z$. **b**, Proposed kinetic growth mode. The first step is nucleation, and the second step is growth. According to the calculations and reported results, all these materials can be thermodynamically synthesized. Therefore, kinetic growth can realize the epitaxial growth of M_aX_b and $M_mP_nX_z$ with controllable phases and compositions, whereas uncontrollable growth produces bulk or particles.

We first discuss the difficulties in the controllable synthesis of 2D materials with multiple phases and multiple compositions. Figure 1a shows the chemical reactions among precursors MCl_x, P and S for preparing M_aX_b and $M_mP_nX_z$. (1) Note that M_aX_b and $M_mP_nX_z$ have different compositions with different phases. According to changes in the Gibbs free energy (taking the Cd-based 2D material in Supplementary Section 1 as an example) and previously reported results (Supplementary Tables 1 and 2), many reactions can take place during chemical vapour deposition (CVD) growth, illustrating that the different compositions and phases of 2D materials (binary M_aX_b and ternary $M_mP_nX_z$) can be thermodynamically obtained and they are competitive with each other. Thus, a controllable chemical reaction is required to realize the compound with a specific composition and tunable phases, such as MX, MX_2 and their hexagonal and tetragonal phases. (2) Similar to—but more complex than—the growth of binary M_aX_b, the chemical reactions during the growth of ternary $M_mP_nX_z$ include binary (M_aX_b, M_cP_d and PS) and ternary reactions. Therefore, the preparation of $M_mP_nX_z$ not only needs to control the reactions for ternary composition growth but also to avoid the formation of binary crystals (M_aX_b, PX and M_cP_d). (3) Meanwhile, some M_aX_b and $M_mP_nX_z$ materials possess non-layered structures, leading to competition between the 2D epitaxial growth (Frank–van der Merwe) and island growth (Stranski–Krastanov) modes[21] (Fig. 1b) during their synthesis; the former growth mode should be controlled for obtaining ultrathin 2D materials.

To address the above challenges, a realization of a direction-controllable growth process is required for controlling the chemical reactions and growth modes. This work proposes a competitive-reaction-based kinetic growth mechanism, which was realized by controlling the growth temperature and vapour pressure. Here the vapour pressure was adjusted by tuning the size of metal precursors. We will analyse the role of precursor size in the mechanism part. Therefore, TMCs and TMPCs with different compositions and defined phases are readily synthesized. Based on this mechanism, more than 60 types are successfully achieved, including 30 TMCs and 21 TMPCs. Most materials (especially all the TMPCs) have not been directly reported with the CVD method. We have also extended the method to successfully synthesize other chalcogenides based on 3*d* transition metals (for example, Cr, Mn and Cu) with different phases.

The corresponding reaction conditions and tailored recipes are detailed in Methods and summarized in Supplementary Fig. 1 and Supplementary Table 3. Supplementary Fig. 2 and Supplementary Section 2 show the phase diagram for CVD growth and examination of each material. Figure 2a shows the summary of optical images of 2D TMCs and TMPCs synthesized by our competitive-reaction-based growth strategy. For typical Fe-based 2D crystals, binary FeX and FeX_2 (X = S, Se and Te) with different phases and ternary $FePX_3$ (X = S, and Se) crystals, as well as their alloys, can be controllably synthesized. Specifically, the two phases of FeX can be achieved by tuning the growth temperature and chalcogen temperature. For example, the two phases of FeS can be obtained by tuning the growth temperature (~600–640 °C) and the S precursor temperature (~120–140 °C). At a low growth temperature, ultrathin non-layered hexagonal FeX was obtained, whereas monolayer tetragonal FeX was achieved at higher temperatures. Meanwhile, by tuning the ratio and temperature of S, Se, Te and metal precursors, the heterostructures and alloys based on hexagonal and tetragonal morphologies were also achieved, which offer a great platform to probe high-temperature 2D magnetism and Majorana bound states[22,23]. Analogous to FeX, FeX_2 crystals and their alloys also possess two different crystal structures, exhibiting the shapes of hexagons, triangles, trapezoids and nanowires. Their synthesis protocol is similar to FeX and the appearance of ultrathin trapezoids and nanowires is attributed to the decomposition and phase transition with an increase in growth temperature. For example, the ultrathin trapezoidal and monolayer triangular shapes of FeS_2 are obtained at a growth temperature of ~640–675 °C and S precursor temperature of ~140–170 °C, whereas one-dimensional FeS_2 nanowires can be obtained at a growth temperature above 675 °C (Fig. 2). The optical images and corresponding Raman spectra are shown in Supplementary Figs. 3–15. The thickness and stability of large-scale FeX and FeX_2 are also studied (Supplementary Figs. 16–19). Supplementary Fig. 7 and Supplementary Figs. 20 and 21 discuss details about the reproducibility and density of FeX and FeX_2 flakes, respectively. Note that changing both metal

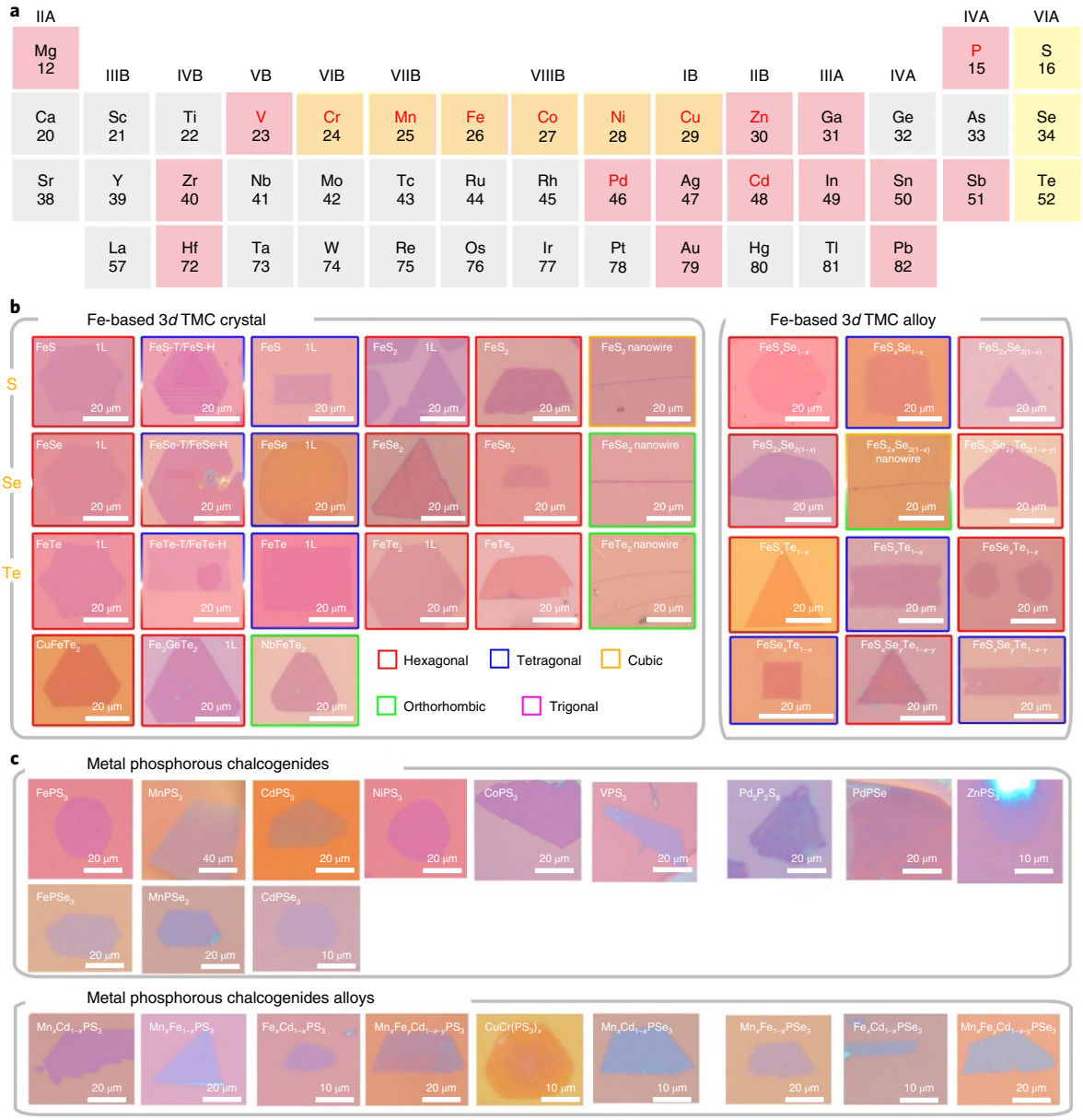

Fig. 2 | Optical images of as-synthesized TMCs and TMPCs. a, Summary of the materials synthesizable using this method. The elements highlighted in red indicate that their metal phosphorous chalcogenides have been obtained via our method, whereas the elements highlighted in black with a pink background indicate that their metal phosphorous chalcogenides should be synthesizable using this method. The elements with an orange background mean that their chalcogenides with different phases have been synthesized using this method. **b**,**c**, Optical images of the as-synthesized 2D materials. These materials include hexagonal, tetragonal, cubic, orthorhombic and trigonal phases (1L: monolayer). Binary crystals: hexagonal phase (FeS, FeSe and FeTe with hexagonal shape; FeS_2, $FeSe_2$ and $FeTe_2$ with hexagonal, triangular or trapezoidal shape), tetragonal phase (FeS, FeSe and FeTe with a rectangular shape), cubic phase (FeS_2 nanowire) and orthorhombic phase ($FeSe_2$ and $FeTe_2$ nanowires). Heterostructures: FeS-H/FeS-T, FeSe-H/FeSe-T, FeTe-H/FeTe-T and FeS_xSe_{1-x}-H/FeS_xSe_{1-x}-T (Supplementary Fig. 8). Alloys (hexagonal phase: FeS_xSe_{1-x}, FeS_xTe_{1-x}, $FeSe_xTe_{1-x}$, $FeS_xSe_yTe_{1-x-y}$, $FeS_{2x}Se_{2(1-x)}$ with the hexagonal shape, $FeS_{2x}Se_{2(1-x)}$ with the trapezoidal shape and $FeS_{2x}Se_{2y}Te_{2(1-x-y)}$; tetragonal phase: FeS_xSe_{1-x}-T, FeS_xTe_{1-x}-T, $FeSe_xTe_{1-x}$-T and $FeS_xSe_yTe_{1-x-y}$-T; cubic or orthorhombic phase: $FeS_{2x}Se_{2(1-x)}$ nanowires). Ternary crystals (Fe_3GeTe_2, $FeCuTe_2$ and $NbFeTe_2$) and phosphorous chalcogenides ($FePS_3$, $MnPS_3$, $CdPS_3$, VPS_3, $NiPS_3$, $ZnPS_3$, $CoPS_3$, $FePSe_3$, $MnPSe_3$, $CdPSe_3$, $Pd_3P_2S_8$, $PdPSe$, $Mn_xFe_{1-x}PS_3$, $Mn_xCd_{1-x}PS_3$, $Fe_xCd_{1-x}PS_3$, $CuCr(PS_3)_x$, $Mn_xFe_{1-x}PSe_3$, $Mn_xCd_{1-x}PSe_3$, $Fe_xCd_{1-x}PSe_3$, $Mn_xFe_yCd_{1-x-y}PS_3$ and $Mn_xFe_yCd_{1-x-y}PSe_3$).

and chalcogen compositions away from the endpoints of Fe-based 2D materials is very important since they should have excellent physical properties. By tuning the temperature of metal chloride and chalcogen, the quantitative compositions of Fe-based 2D materials can be controllably synthesized (Supplementary Fig. 22). Furthermore, a large-scale film was also synthesized and discussed (Supplementary Fig. 23).

Similarly, TMPCs have more than five different chemical compositions: MPX, MPX_3, MPX_4, $M(PX_3)_2$ and $M_3P_2X_8$ (ref. [24]). With our proposed growth mechanism, ultrathin MPX, MPX_3 and $M_3P_2X_8$ are successfully synthesized, including 13 crystals and 8 alloys. The corresponding optical images and Raman spectroscopy data are shown in Supplementary Figs. 24–31. Notably, MPX_3-based alloys can be achieved by tuning the metal precursor ratio (Supplementary

Fig. 32) and are similar to the growth conditions of Fe-based alloys. Furthermore, the prepared Cr-, Mn-, Co-, Ni- and Cu-based 2D materials with different compositions further demonstrate the universality of our growth method (Supplementary Figs. 33–35). The detailed thicknesses of Fe-based 2D materials and typical MPX_3 are shown in Supplementary Fig. 36.

Next, we focus on the growth mechanism of the proposed method. Here we take $Fe(P)S_x$ as an example since others have a similar growth process. Figure 3a illustrates the growth of these materials through the interaction between $FeCl_2$ molecules and S/P vapours. Note that the changes in Gibbs free energy show that the formation of Fe-based binary (ternary) crystals is thermodynamically favourable (Supplementary Section 3.1). However, the competitive chemical reactions during binary (ternary) crystal growth cannot be controlled when small-sized nanoparticle chlorides are used as the precursors[25,26]. This is attributed to the fact that the high evaporation rate of the small-sized precursor (especially for sizes less than ~50 nm) leads to high reactivity (Fig. 3a, steps 1–3) and thus satisfies the reactions for most Fe-based crystals. Therefore, nucleation and growth cannot be controlled. Figure 3b shows the evidence that many nuclei of $Fe(P)X_y$ were generated and large-sized particles were obtained (Fe_xS_y with different phases, Fe_xP and $FePS_y$ $Fe_x(P)S_y$ particles (Supplementary Fig. 37 shows the scanning electron microscopy image and energy-dispersive X-ray spectroscopy (EDS) results) are preferable). This is attributed to the fact that the uncontrolled reactions induced by the high partial vapour pressure leads to the island growth (Fig. 3a, step 3). Thus, we can conclude that the nucleation and growth rate of a single phase is a kinetics-determined process rather than a thermodynamically determined one. To control the growth kinetics and realize a specific chemical reaction, large-sized precursors with low vapour pressure were used, which help to regulate the competitive reactions for the single-phase growth of a specific material in terms of nucleation and epitaxial growth (Fig. 3a, steps 4–6). Therefore, ultrathin 2D crystals (such as FeS_x and $FePS_3$) can be obtained by using large-sized $FeCl_2$ precursors (Fig. 3a, steps 4–6).

The thermogravimetric analysis (TGA) shown in Fig. 3c further demonstrates that at low temperatures, $FeCl_2$ nanoparticles are much easier to evaporate than $FeCl_2$ bulk; evidently, small-sized precursors (red curves) evaporate much faster than large-sized ones (black curves) at lower temperatures. As a result, the chemical reaction for a specific phase cannot be controlled due to the high partial vapour pressure. Meanwhile, the formation of excessive nuclei and the resulting island growth mode with uncontrollable compositions hinder the crystallization of single-phase $Fe(P)X_y$ (Supplementary Figs. 40 and 41). In contrast, large-sized precursors with a low partial vapour pressure can be easily tuned for specific material growth and significantly reduce the nucleation density and promote the growth with the Frank–van der Merwe mode, thereby facilitating the crystallization of TMCs and TMPCs. Supplementary Section 3.4 provides the effect of precursor size as well as detailed discussions. Supplementary Information discusses the kinetics of nucleation under different growth conditions (Supplementary Figs. 40–47).

We further analyse the effects of growth kinetics on compositions and phases. Fe-based crystals can be classified into two different chemical compositions (TMCs, FeX and FeX_2; TMPCs, FePX and $FePX_3$) and each composition has several different phases. The competitive chemical reactions among these compositions and phases can be controlled by adjusting the vapour pressures of $FeCl_2$, S and P via the reaction temperature since they have different formation energies. For instance, $FeCl_2$ at higher temperatures (~650–675 °C) can form FeX_2, whereas lower temperatures (~580–650 °C) can produce FeS and $FePS_3$. The established growth phase diagram is shown in Fig. 3d. Note that the amount of metal precursors is sufficiently maintained during the reactions and cannot affect the phase and composition of Fe-based 2D materials in a short growth time.

Density functional theory (DFT) calculations were performed to reveal the competitive chemical reaction mechanism of TMCs[27]. Supplementary Section 3 shows the chemical-reaction formation energy of FeX_y and their alloys. Supplementary Figs. 48–51 discuss the DFT calculations for both FeS and FeS_2. Accordingly, the chemical-reaction-based transformation of FeS to FeS_2 can be realized by tuning the critical partial pressure and S species. The free energies of S_2/S_8 gases depending on the partial pressure and temperature are shown in Fig. 3e,f. The critical partial pressure for S_2 gas to transform FeS to FeS_2 at 900 K is ~1 Pa, whereas the critical partial pressure for S_8 gas is higher than 1 atm. Therefore, tuning the vapour pressure of S and $FeCl_2$ can control the competitive chemical reactions between FeX and FeX_2 phases (Supplementary Section 3.4). The calculation regarding the chemical transition from FeS to FeS_2 matches with the experimental observation, where FeS grows at a low temperature and FeS_2 grows at a high temperature with different vapour pressures of the precursor. Supplementary Figs. 50 and 51 discuss more calculations about the alloys ($FeS_{2x}Se_{2(1-x)}$ and FeS_xSe_{1-x}), which show that $FeS_{2x}Se_{2(1-x)}$ or FeS_xSe_{1-x} with any composition can be synthesized by tuning the supply of S and Se.

The atomic structures and chemical compositions of the as-synthesized 2D crystals are further uncovered by aberration-corrected scanning transmission electron microscopy–annular dark-field (STEM-ADF) imaging, EDS and electron energy loss spectroscopy (EELS). Since it is challenging to transfer monolayer 2D 3*d* crystals onto TEM grids, we mainly focus on the characterization of few-layer 2D Fe-based samples and TMPCs with identical crystal structures. According to the combined analysis of experimental and simulated *Z*-contrast STEM images, EDS mapping and EELS results, most of the obtained Fe-based chalcogenides and TMPCs are confirmed to belong to five different space groups (Supplementary Fig. 46), which are classified into five categories here: (1) $P6_3/mmc$ (non-layered FeX with hexagonal/triangular shape); (2) $P4/nmm$ (layered FeX with tetragonal shape); (3) $P\bar{3}m1$ (layered FeX_2 with hexagonal/triangular/trapezoidal shape); (4) $Pa\bar{3}$ (non-layered FeS_2 nanowires) and $Pmnn$ (non-layered $FeSe_2$ and $FeTe_2$ nanowires); (5) $C2/m$ (MPX_3, M = Mg, V, Cr, Mn, Fe, Co, Ni, Ag, Cd or Zn). For clarifications, we select FeS_x and some TMPCs to demonstrate the diversity and controllability of the crystal structures. Figure 4a shows a typical atomic-resolution STEM-ADF image of a hexagonal-shaped FeS crystal along the [001] zone axis, where the high-contrast (brighter) and low-contrast (darker) spots represent the Fe and S atom columns, respectively, as aligned with the atomic structure model. The sharp dots in the fast Fourier transform (FFT) patterns (Fig. 4a–l, insets) obtained from the corresponding larger area further suggest the single crystallinity of the flake and exhibit the hexagonal symmetry feature of the $P6_3/mmc$ lattice. In comparison, the STEM-ADF image together with the FFT pattern (Fig. 4b, inset) demonstrates that a tetragonal-shaped FeS crystal possesses a distinct atomic arrangement, where each Fe (S) atom coordinates with four S (Fe) atoms belonging to the $P4/nmm$ space group. Similar to FeS, FeS_2 also has two different atomic structures: $P\bar{3}m1$ and $Pa\bar{3}$ (Fig. 4c,d, respectively). Note that hexagonal/triangular FeS ($P6_3/mmc$) and FeS_2 ($P\bar{3}m1$) have resembling structures. Their difference can be unambiguously recognized from the contrast ratio of Fe to S atom columns of the STEM-ADF images and EDS stoichiometry (Supplementary Figs. 53–56). The structure and STEM-ADF image analysis of FeS (FeS_2) are presented in Supplementary Fig. 57. Similarly, $FeSe_x$ and $FeTe_x$ present similar crystal structures to FeS_x (Fig. 4e–g,i–k), except for the fact that $FeSe_2$ and $FeTe_2$ nanowires belong to the $Pmnn$ space group rather than $Pa\bar{3}$ (Fig. 4h,l). Supplementary Figs. 53–76 provide a detailed analysis.

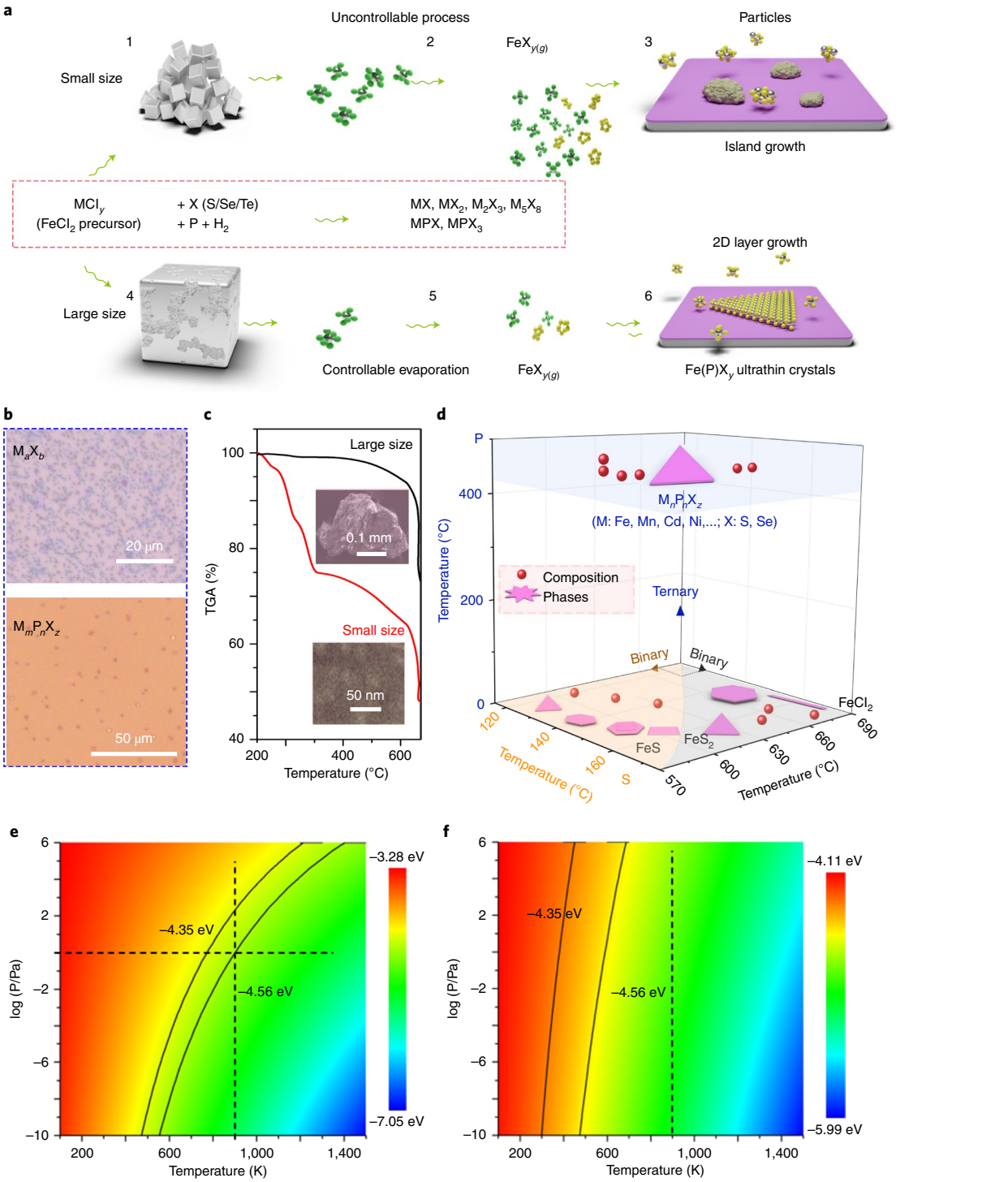

Fig. 3 | Growth mechanism of 3*d*-metal-based 2D materials. a, Growth mechanism of Fe(P)X_y. The red dotted frame shows the possible products formed by the reactions between MCl_y and X/P. Steps 1–6 show an example in which $FeCl_2$ is used as the precursor. The Fe-based precursors with small and large sizes result in the formation of Fe-based nanoparticles and ultrathin crystals, respectively. Larger-sized $FeCl_2$ particles can generate less vapour and react with chlorides to form Fe(P)X_y molecules, which then grow on the substrate. **b**, Nanoparticles are obtained if the growth process of Fe(P)X_y is uncontrollable in kinetics. **c**, TGA of $FeCl_2$ precursors with different sizes. The black curve corresponds to the weight-loss curve when using large-sized precursors, whereas the red curve demonstrates the weight-loss curve using small-sized precursors. It can be clearly seen that precursors with a size larger than 0.1 mm have a low evaporation rate, whereas precursors with a small size are quickly evaporated, resulting in excess precursors. The quick weight loss at temperatures lower than 300 °C is attributed to the evaporation of absorbed water. **d**, Growth diagram of Fe(P)X_y with different temperatures of S and P, and growth temperature. **e**,**f**, Free energy of S_2 (**e**) and S_8 (**f**) gas as a function of their partial pressure and temperature. The solid line shows the isochemical potential and the dashed line shows the vapour pressure of S at 900 K. The isoline (solid line) at −4.35 and −4.56 eV per S atom is given. The critical partial pressure for S_2 gas to transform multilayer FeS into multilayer FeS_2 at 900 K (dashed line) is ~1 Pa, whereas the critical partial pressure for S_8 gas is higher than 1 atm. Obviously, the transformation from multilayer FeS to multilayer FeS_2 should be mediated by S molecules smaller than S_8.

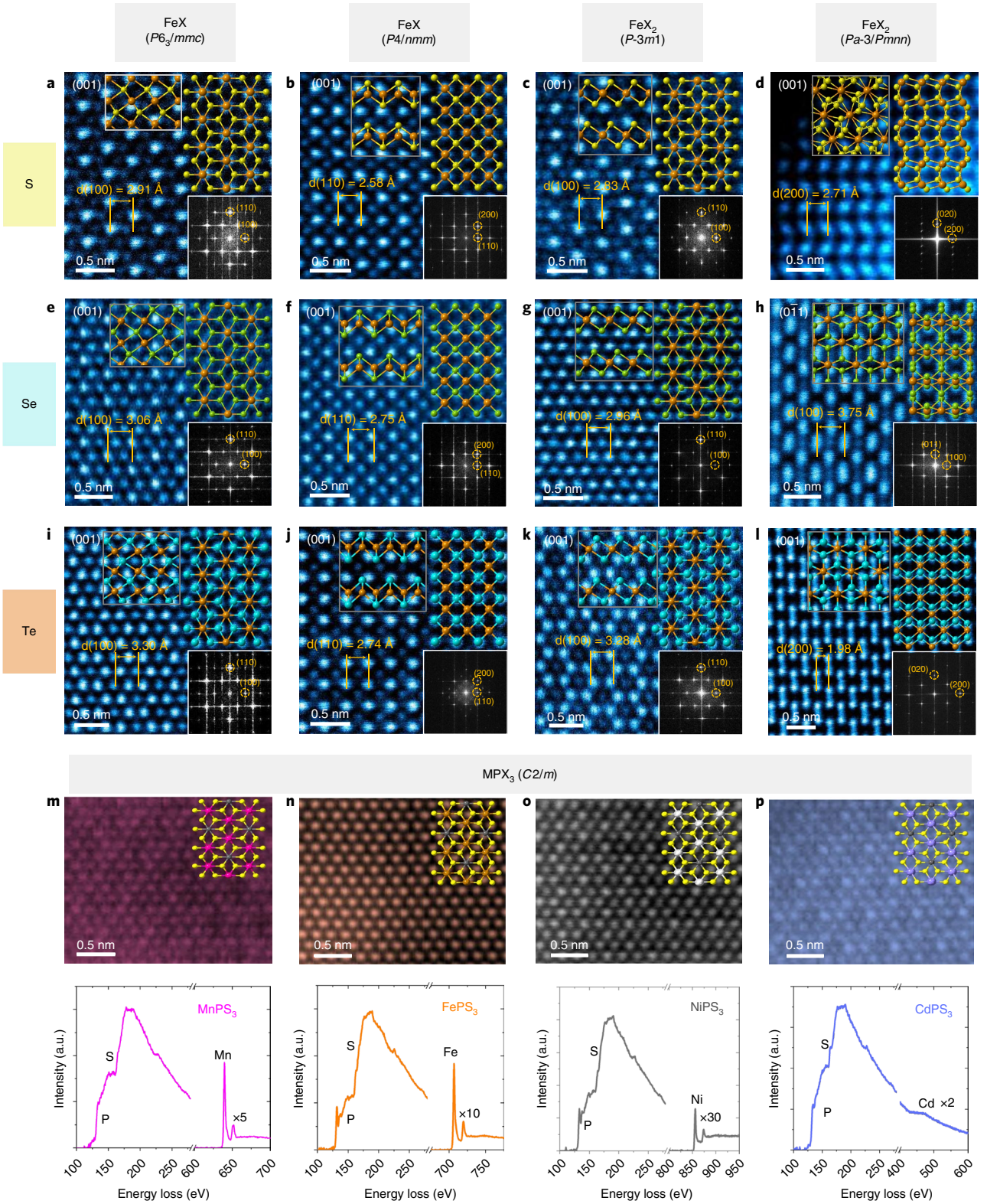

Fig. 4 | STEM characterizations of the as-synthesized 2D materials. a,**e**,**i**, STEM-ADF images of FeS (**a**), FeSe (**e**) and FeTe (**i**) with a hexagonal/triangular shape. The insets display the top and side views of the atomic structure models as well as the FFT patterns, showing that non-layered hexagonal/triangular FeX belongs to the $P6_3/mmc$ space group. **b**,**f**,**j**, STEM-ADF images of FeS, FeSe and FeTe with a tetragonal shape. The insets display the top and side views of the atomic structure models as well as the FFT patterns, showing that layered tetragonal FeX belongs to the $P4/nmm$ space group. **c**,**g**,**k**, STEM-ADF images of FeS_2, $FeSe_2$ and $FeTe_2$ with a hexagonal/triangular/trapezoidal shape. The insets display the top and side views of the atomic structure models as well as the FFT patterns, showing that layered hexagonal/triangular/trapezoidal FeX_2 belongs to the $P\bar{3}m1$ space group. **d**,**h**,**l** STEM-ADF images of FeS_2, $FeSe_2$ and $FeTe_2$ nanowires. The insets display the top and side views of the atomic structure models as well as the FFT patterns, showing that non-layered FeX_2 belongs to the $Pa\bar{3}$ (FeS_2 nanowire) and $Pmnn$ ($FeSe_2$ and $FeTe_2$ nanowires) space groups. **m**–**p**, STEM-ADF images of layered $MnPS_3$ (**m**), $FePS_3$ (**n**), $NiPS_3$ (**o**) and $CdPS_3$ (**p**) and the corresponding EELS spectra, illustrating that MPS_3 belong to the $C2/m$ space group.

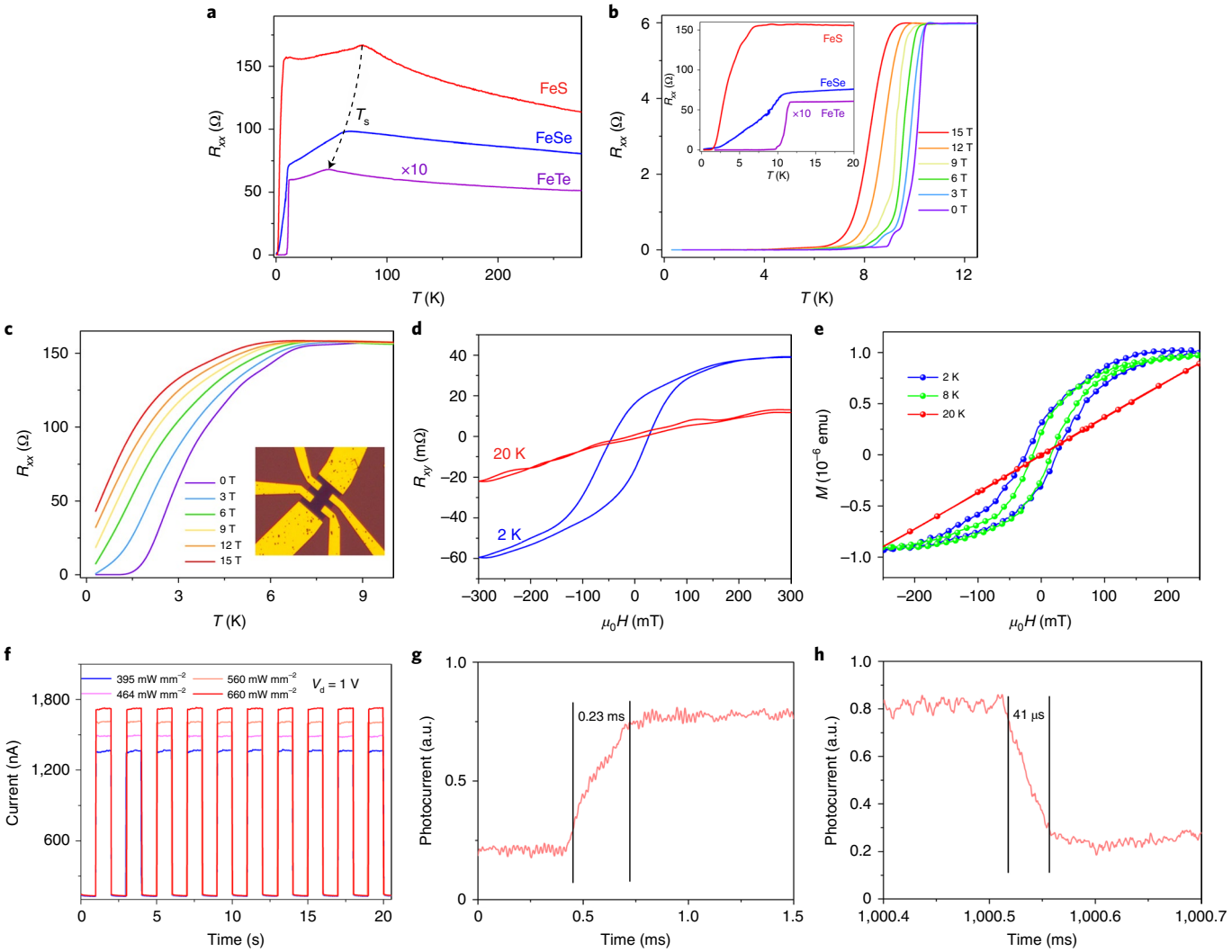

Fig. 5 | Physical properties of selected Fe-based TMCs by tuning the compositions. a, Temperature dependence of longitudinal resistances of few-layer FeS, FeSe and FeTe with the tetragonal phase. For clarity, the data for FeTe have been magnified ten times. T_s represents the characteristic temperature corresponding to a structural/magnetic transition. **b**,**c**, Temperature evolution of longitudinal resistance R_{xx} in various perpendicular magnetic fields (H) of 0, 3, 6, 9, 12 and 15 T below 10 K for FeTe (**b**) and FeS (**c**). The inset in **b** displays a zoomed-in view of the superconducting region, and the inset in **c** shows a typical device used for low-temperature magnetotransport measurements. **d**,**e**, Magnetoresistance (**d**) and magnetization (M) (**e**) measurements performed at several fixed temperatures. A clear hysteresis is observed, demonstrating that the ferromagnetic order forms at low temperatures ($T < 20$ K). The T_c value of FeS_2 is about 15 K. μ_0 is the magnetic permeability of vacuum. **f**, Performance of typical few-layer $FeTe_2$ infrared photodetectors under 940 nm laser illumination with different laser powers. V_d is the applied voltage of $FeTe_2$ infrared photodetectors. **g**,**h**, Response time of the single-cycle response of light on (**g**) and light off (**h**). The rise and fall times are about 230 and 41 μs, respectively.

Figure 4m–p shows the atomic-resolution STEM-ADF images and the corresponding EELS data of $MnPS_3$, $FePS_3$, $NiPS_3$ and $CdPSe_3$, respectively. Structurally, the primary unit cell of monolayer MPX_3 is composed of one dumbbell-shaped P_2X_6 atom packing and two M atoms, forming a honeycomb structure with each M atom coordinating with six X atoms and each P atom coordinating with one P and three X atoms[28]. When stacked along the vertical direction, the interplane displacement between the MPX_3 layers breaks the three-fold inversion rotation symmetry to generate a monoclinic lattice belonging to the $C2/m$ space group. The STEM-ADF images of these four as-synthesized TMPCs manifest a six-fold symmetry lattice along the [103] zone axis, consistent with the characteristics of both hexagonal monolayer and monoclinic stacking for multilayer MPX_3. Besides, the EELS spectrum reveals the core-loss singles of Mn $L_{2,3}$ edge, Fe $L_{2,3}$ edge, Ni $L_{2,3}$ edge and Cd $M_{4,5}$ edge for the corresponding samples, confirming the element component of MPX_3. Supplementary Figs. 77 and 78 show the structures and energy bands of some materials.

More importantly, these 2D materials exhibit fascinating physical properties[14,29,30], making them an emerging platform for fundamental studies and practical applications. However, tuning these properties through their compositions and phases is still challenging. Based on this growth mechanism, the compositions of 2D materials are well controlled. Figure 5a presents the temperature dependence of longitudinal resistance $R_{xx}(T)$ of FeX with a tetragonal phase. All the three samples showed a semiconductor-like behaviour, that is, R_{xx} increases with decreasing temperature. However, when the temperature is further reduced to around 70 K, a gradual crossover to a metallic conducting behaviour is found due to a structural phase transition accompanied by a magnetic transition[31–35]. Interestingly, we find that T_s decreases from 80 K for 1T-FeS, 63 K for 1T-FeSe and 49 K

for 1T-FeTe. The metallic characteristics persist down to about 10 K; then, $R_{xx}(T)$ drops to zero, indicating the onset of superconductivity in tetragonal FeX. For clarity, Fig. 5b, inset, shows the zoomed-in view of the superconducting region. We find that the T_c values of FeS, FeSe and FeTe are 3.3, 7.3 and 11.0 K, respectively, when the midpoint of the resistive transition is selected as the superconducting transition temperature T_c. The temperature evolution of longitudinal resistance $R_{xx}(H)$ under different magnetic fields (Fig. 5b,c) further confirms the superconducting transition. Supplementary Fig. 79a,b shows more evidence and discussions of superconductivity[36,37]. Supplementary Fig. 80 discusses the properties of hexagonal FeX. In our experiment, both three-dimensional pyrite FeS_2 and layered FeS_2 were obtained. Notably, for three-dimensional pyrite FeS_2, it has been predicted that the (111)-oriented three-atom-thick sheets have a stable ferromagnetic ground state[38]. However, to the best of our knowledge, there is no report about the property of layered FeS_2 monolayer. Furthermore, 2D ferromagnetism was observed in layered FeX_2 monolayer in our work (Supplementary Fig. 36). The external magnetic field (H)-dependent Hall electrical resistivities (ρ_{xy}) of monolayer FeS_2 at different temperatures are shown in Fig. 5d,e, and the T_c value of FeS_2 is about 15 K, which is different from the predicted value for pyrite FeS_2. Supplementary Table 5 shows a comparison of different 2D magnets. Meanwhile, FeX_2 has a small bandgap, showing the potential applications in catalysis and photodetectors. Few-layer FeS shows a good hydrogen evolution reaction property (Supplementary Fig. 81). Figure 5f shows the performance of typical $FeTe_2$ infrared photodetectors under 940 nm laser illumination with different laser powers. The photocurrent increases with the laser power. Figure 5g,h shows the response speed of the $FeTe_2$ infrared photodetector (10–90% photocurrent change for rise times and 90–10% for fall times). The rise and fall times are about 230 and 41 µs, respectively, better than most of the reported 2D TMDs. Supplementary Fig. 82 shows more results about FeX_2 photodetectors. Supplementary Table 6 provides a comparison of Fe-based materials, with their structures and properties. Additionally, we study the antiferromagnetic properties of MPX_3. Second-harmonic generation (SHG) has been demonstrated to be a direct probe to the long-range antiferromagnetic orders and domains. The corresponding SHG properties of MPX_3 are shown in Supplementary Fig. 83. The temperature-dependent SHG intensity of $MnPS_3$ (Supplementary Fig. 84) demonstrates its antiferromagnetic property. These illustrate the high quality of as-synthesized 2D materials with different compositions and show the platform to study physical properties and construct the ferromagnetism–superconductivity heterostructures.

In conclusion, we have demonstrated a general competitive-chemical-reaction-controlled CVD method for producing TMC and TMPC libraries. In total, 63 compounds and 4 heterostructures with different compositions and phases have been prepared. Our work not only opens a route to synthesize atom-thin TMCs and TMPCs but also demonstrates a novel growth mechanism, which is important for a comprehensive understanding of the growth mechanism of 2D materials. The prepared crystals with controllable phases and compositions as well as heterostructures will offer possibilities to explore physical phenomena, including 2D phase transitions, 2D ferromagnetism, 2D superconductivity, Majorana bound states, spintronics and many-body excitons.

Online content

Any methods, additional references, Nature Research reporting summaries, source data, extended data, supplementary information, acknowledgements, peer review information; details of author contributions and competing interests; and statements of data and code availability are available at https://doi.org/10.1038/s41563-022-01291-5.

Received: 5 June 2021; Accepted: 17 May 2022;
Published online: 23 June 2022

References

1. Schaibley, J. R. et al. Valleytronics in 2D materials. *Nat. Rev. Mater.* **1**, 16055 (2016).
2. Radisavljevic, B., Radenovic, A., Brivio, J., Giacometti, V. & Kis, A. Single-layer MoS_2 transistors. *Nat. Nanotechnol.* **6**, 147–150 (2011).
3. Kang, K. et al. High-mobility three-atom-thick semiconducting films with wafer-scale homogeneity. *Nature* **520**, 656–660 (2015).
4. Zhou, J. et al. A library of atomically thin metal chalcogenides. *Nature* **556**, 355–359 (2018).
5. Lee, Y. H. et al. Synthesis of large-area MoS_2 atomic layers with chemical vapor deposition. *Adv. Mater.* **24**, 2320–2325 (2012).
6. Kang, L. et al. Phase-controllable growth of ultrathin 2D magnetic FeTe crystals. *Nat. Commun.* **11**, 3729 (2020).
7. Zhang, Y. et al. Ultrathin magnetic 2D single-crystal CrSe. *Adv. Mater.* **31**, e1900056 (2019).
8. Chu, J. et al. Sub-millimeter-scale growth of one-unit-cell-thick ferrimagnetic Cr_2S_3 nanosheets. *Nano Lett.* **19**, 2154–2161 (2019).
9. Meng, L. et al. Anomalous thickness dependence of Curie temperature in air-stable two-dimensional ferromagnetic 1T-$CrTe_2$ grown by chemical vapor deposition. *Nat. Commun.* **12**, 809 (2021).
10. Ma, H. et al. Phase-tunable synthesis of ultrathin layered tetragonal CoSe and nonlayered hexagonal CoSe nanoplates. *Adv. Mater.* **31**, e1900901 (2019).
11. Chen, S., Liu, H., Chen, F., Zhou, K. & Xue, Y. Synthesis, transfer, and properties of layered $FeTe_2$ nanocrystals. *ACS Nano* **14**, 11473–11481 (2020).
12. Shivayogimath, A. et al. A universal approach for the synthesis of two-dimensional binary compounds. *Nat. Commun.* **10**, 2957 (2019).
13. Zhao, B. et al. Synthetic control of two-dimensional $NiTe_2$ single crystals with highly uniform thickness distributions. *J. Am. Chem. Soc.* **140**, 14217–14223 (2018).
14. Hsu, F. C. et al. Superconductivity in the PbO-type structure α-FeSe. *Proc. Natl Acad. Sci. USA* **105**, 14262–14264 (2008).
15. Gudelli, V. K., Kanchana, V., Vaitheeswaran, G., Valsakumar, M. C. & Mahanti, S. D. Thermoelectric properties of marcasite and pyrite FeX_2 (X = Se, Te): a first principle study. *RSC Adv.* **4**, 9424–9431 (2014).
16. Deng, Y. et al. Gate-tunable room-temperature ferromagnetism in two-dimensional Fe_3GeTe_2. *Nature* **563**, 94–99 (2018).
17. Wang, D. et al. Evidence for Majorana bound states in an iron-based superconductor. *Science* **362**, 333–335 (2018).
18. Kong, L. et al. Half-integer level shift of vortex bound states in an iron-based superconductor. *Nat. Phys.* **15**, 1181–1187 (2019).
19. Bansal, D. et al. Magnetically driven phonon instability enables the metal–insulator transition in h-FeS. *Nat. Phys.* **16**, 669–675 (2020).
20. Kang, S. et al. Coherent many-body exciton in van der Waals antiferromagnet $NiPS_3$. *Nature* **583**, 785–789 (2020).
21. Li, H., Li, Y., Aljarb, A., Shi, Y. & Li, L. J. Epitaxial growth of two-dimensional layered transition-metal dichalcogenides: growth mechanism, controllability, and scalability. *Chem. Rev.* **118**, 6134–6150 (2018).
22. Zhang, P. et al. Multiple topological states in iron-based superconductors. *Nat. Phys.* **15**, 41–47 (2018).
23. Wang, Z. et al. Evidence for dispersing 1D Majorana channels in an iron-based superconductor. *Science* **367**, 104–108 (2020).
24. Gusmao, R., Sofer, Z. & Pumera, M. Metal phosphorous trichalcogenides ($MPCh_3$): from synthesis to contemporary energy challenges. *Angew. Chem. Int. Ed.* **58**, 9326–9337 (2019).
25. Cain, J. D., Shi, F., Wu, J. & Dravid, V. P. Growth mechanism of transition metal dichalcogenide monolayers: the role of self-seeding fullerene nuclei. *ACS Nano* **10**, 5440–5445 (2016).
26. Zhu, D. et al. Capture the growth kinetics of CVD growth of two-dimensional MoS_2. *npj 2D Mater. Appl.* **1**, 8 (2017).
27. Li, S. et al. Vapour–liquid–solid growth of monolayer MoS_2 nanoribbons. *Nat. Mater.* **17**, 535–542 (2018).
28. Long, G. et al. Isolation and characterization of few-layer manganese thiophosphite. *ACS Nano* **11**, 11330–11336 (2017).
29. Kamihara, Y., Watanabe, T., Hirano, M. & Hosono, H. Iron-based layered superconductor $La[O_{(1-x)}F_x]FeAs$ ($x = 0.05–0.12$) with $T_c = 26$ K. *J. Am. Chem. Soc.* **130**, 3296–3297 (2008).
30. Mizuguchi, Y., Tomioka, F., Tsuda, S., Yamaguchi, T. & Takano, Y. Superconductivity at 27 K in tetragonal FeSe under high pressure. *Appl. Phys. Lett.* **93**, 152505 (2008).
31. Si, W. et al. Superconductivity in epitaxial thin films of $Fe_{1.08}Te:O_x$. *Phys. Rev. B* **81**, 092506 (2010).
32. Margadonna, S. et al. Crystal structure of the new $FeSe_{(1-x)}$ superconductor. *Chem. Commun.* **2008**, 5607–5609 (2008).

33. McQueen, T. M. et al. Tetragonal-to-orthorhombic structural phase transition at 90 K in the superconductor $Fe_{1.01}Se$. *Phys. Rev. Lett.* **103**, 057002 (2009).
34. Li, S. et al. First-order magnetic and structural phase transitions in$Fe_{1+y}Se_xTe_{1-x}$. *Phys. Rev. B* **79**, 054503 (2009).
35. Kuhn, S. J. et al. Structure and property correlations in FeS. *Phys. C Supercond. Appl.* **534**, 29–36 (2017).
36. Terashima, T. et al. Upper critical field and quantum oscillations in tetragonal superconducting FeS. *Phys. Rev. B* **94**, 100503 (2016).
37. Lai, X. et al. Observation of superconductivity in tetragonal FeS. *J. Am. Chem. Soc.* **137**, 10148–10151 (2015).
38. Puthirath, A. B. et al. Apparent ferromagnetism in exfoliated ultrathin pyrite sheets. *J. Phys. Chem. C* **125**, 18927–18935 (2021).

Methods

Synthesis recipe. The 2D compounds and heterostructures were synthesized in a quartz tube (diameter, one inch). The length of the furnace is about 36 cm (Supplementary Fig. 1). Specifically, the alumina boat with a volume of ~8.0 cm × 1.1 cm × 0.6 cm containing the precursor powder was put in the centre of the tube. The corresponding MCl_2 or mixed MCl_2 with a large size was used as the precursor. Si/SiO_2 was placed on the alumina boat with the surface facing down. The distance between the precursor source and substrate is about 0.2–0.3 cm. Another alumina boat containing S, Se or Te powder was put upstream of the tube furnace at ~120–200, ~220–300 and ~450–500 °C, respectively. The heating rate of all the reactions is 50 °C min^{-1}. All the reactions were carried out at atmospheric pressure. The growth time of the Fe-based binary is 1 min and Ar/H_2 gas at a flow rate of 120/6 s.c.c.m. was used as the carrier gas without any specific description. The temperature was cooled down to room temperature by blowing a fan. All the reaction materials were bought from Alfa Aesar with purity of more than 99%.

FeS-H (FeS-T). $FeCl_2$ (2 mg for FeS-H and 5 mg for FeS-T) in an alumina boat was placed in the centre of the tube. The furnace was heated to the growth temperature (600–620 °C for FeS-H and 630–640 °C for FeS-T). The heating temperature of S (2 and 4 mg) is 120 and 140 °C, respectively.

FeS-H/FeS-T. $FeCl_2$ (4 mg) in an alumina boat was placed in the centre of the tube. The furnace was heated to the growth temperature (~620–630 °C). The heating temperature of S (2 mg) is 130 °C.

FeS_2-(trapezoidal (cubic) shape). $FeCl_2$ (5 mg) in an alumina boat was placed in the centre of the tube. The furnace was heated to the growth temperature (660–675 and 675–750 °C for the trapezoidal and cubic phase, respectively). The heating temperature of S (2 and 4 mg) is 160 and 170 °C, respectively.

FeS_2-(hexagonal/triangular shape). $FeCl_2$ (2 mg) in an alumina boat was placed in the centre of the tube. The furnace was heated to the growth temperature (640–660 °C). The heating temperature of S (2 mg) is 165 °C.

FeSe-H (FeSe-T). $FeCl_2$ (2 mg for FeSe-H and 5 mg for FeSe-T) in an alumina boat was placed in the centre of the tube. The furnace was heated to the growth temperature (600–620 and 630–640 °C for FeSe-H and FeSe-T, respectively). The heating temperature of Se (2 and 4 mg, respectively) is 220 and 230 °C, respectively.

FeSe-H/FeSe-T. $FeCl_2$ (3 mg) in an alumina boat was placed in the centre of the tube. The furnace was heated to the growth temperature of 620–630 °C. The heating temperature of Se (2 mg) is 230 °C.

$FeSe_2$-(trapezoidal (hexagonal/triangular) shape). $FeCl_2$ (5, 5 and 3 mg for the trapezoidal, orthorhombic and hexagonal/triangular shape, respectively) in an alumina boat was placed in the centre of the tube. The furnace was heated to the growth temperature (660–675, 675–750 and 640–660 °C for the trapezoidal, orthorhombic and hexagonal/triangular shape, respectively). The heating temperature of Se (4 and 2 mg, respectively) is 240 and 250 °C, respectively.

FeTe-H (FeTe-T). $FeCl_2$ (2 and 5 mg for FeTe-H and 5 mg for FeTe-T) in an alumina boat was placed in the centre of the tube. The furnace was heated to the growth temperature (600–620 and 630–640 °C for FeTe-H and FeTe-T, respectively). The heating temperature of Te (5 and 10 mg, respectively) is 450 and 470 °C, respectively.

FeTe-H/FeS-T. $FeCl_2$ (5 mg) in an alumina boat was placed in the centre of the tube. The furnace was heated to the growth temperature (620–630 °C). The heating temperature of Te (10 mg) is 450 °C.

$FeTe_2$-(trapezoidal (hexagonal/triangular) shape). $FeCl_2$ (5 and 3 mg for the trapezoidal and hexagonal/triangular shape) in an alumina boat was placed in the centre of the tube. The furnace was heated to the growth temperature (650–675 and 640–650 °C for the trapezoidal and hexagonal/triangular shape, respectively). The heating temperature of Te (10 mg) is 480 °C.

$FeTe_2$-(orthorhombic shape). $FeCl_2$ (5 mg) in an alumina boat was placed in the centre of the tube. The furnace was heated to the growth temperature (675–750 °C). The heating temperature of Te (10 mg) is 500 °C.

FeS_xSe_{1-x}-H (FeS_xSe_{1-x}-T). $FeCl_2$ (3 and 5 mg for FeS_xSe_{1-x}-H and FeS_xSe_{1-x}-T, respectively) in an alumina boat was placed in the centre of the tube. The furnace was heated to the growth temperature (600–620 and 630–640 °C for FeS_xSe_{1-x}-H and FeS_xSe_{1-x}-T, respectively). The heating temperature of mixed S and Se (2 mg) is 140 °C.

FeS_xSe_{1-x}-H/FeS_xSe_{1-x}-T. $FeCl_2$ (5 mg) in an alumina boat was placed in the centre of the tube. The furnace was heated to the growth temperature (620–630 °C). The heating temperature of mixed S and Se (4 mg) is 150 °C.

$FeS_{2x}Se_{2(1-x)}$-(trapezoidal shape). $FeCl_2$ (5 mg) in an alumina boat was placed in the centre of the tube. The furnace was heated to the growth temperature (650–675 °C). The heating temperature of mixed S and Se (4 mg) is 180 °C.

$FeS_{2x}Se_{2(1-x)}$-(hexagonal/triangular shape). $FeCl_2$ (3 mg) in an alumina boat was placed in the centre of the tube. The furnace was heated to the growth temperature (640–650 °C). The heating temperature of mixed S and Se (4 mg) is 200 °C.

$FeS_{2x}Se_{2(1-x)}$-(cubic/orthorhombic shape). $FeCl_2$ (5 mg) in an alumina boat was placed in the centre of the tube. The furnace was heated to the growth temperature (660–750 °C). The heating temperature of mixed S and Se (4 mg) is 200 °C.

FeS_xTe_{1-x}-H. $FeCl_2$ (2 mg) in an alumina boat was placed in the centre of the tube. The furnace was heated to the growth temperature (630–640 °C). The heating temperature of mixed S and Te (10 mg) is 450 °C.

FeS_xTe_{1-x}-T. $FeCl_2$ (5 mg) in an alumina boat was placed in the centre of the tube. The furnace was heated to the growth temperature (640–650 °C). The heating temperature of mixed S and Te (10 mg) is 470 °C.

$FeSe_xTe_{1-x}$-H. $FeCl_2$ (5 mg) in an alumina boat was placed in the centre of the tube. The furnace was heated to the growth temperature (600–630 °C). The heating temperature of mixed Se and Te (10 mg) is 450 °C.

$FeSe_xTe_{1-x}$-T. $FeCl_2$ (5 mg) in an alumina boat was placed in the centre of the tube. The furnace was heated to the growth temperature (640–650 °C). The growth time is 1 min. The heating temperature of mixed Se and Te (10 mg) is 470 °C.

$FeS_xSe_yTe_{1-x-y}$-H. $FeCl_2$ (2 mg) in an alumina boat was placed in the centre of the tube. The furnace was heated to the growth temperature (610–630 °C). The heating temperature of S/Se (2 mg) and Te (10 mg) is 130 and 450 °C, respectively.

$FeS_xSe_yTe_{1-x-y}$-T. $FeCl_2$ (5 mg) in an alumina boat was placed in the centre of the tube. The furnace was heated to the growth temperature (630–650 °C). The growth time is 1 min. The heating temperature of mixed S/Se (2 mg) and Te (10 mg) is 150 and 470 °C, respectively.

$FeS_{2x}Se_{2y}Te_{2(1-x-y)}$-(trapezoidal shape). $FeCl_2$ (5 mg) in an alumina boat was placed in the centre of the tube. The furnace was heated to the growth temperature (650–675 °C). The heating temperature of mixed S/Se (2 mg) and Te (10 mg) is 170 and 480 °C, respectively.

Fe_3GeTe_2 ($FeNbTe_2$/$FeCuTe_2$). The pressed 10 mg mixed $FeCl_2$/GeI_2 ($FeCl_2$/$NbCl_5$ or $FeCl_2$/$CuCl_2$) powder in an alumina boat was placed in the centre of the tube. The furnace was heated to the growth temperature (580–600 °C for Fe_3GeTe_2 and 600–700 °C for $FeNbTe_2$ and $FeCuTe_2$). The heating temperature of Te (10 mg) is 500 °C.

$FePS_3$ ($MnPS_3$ and $CdPS_3$). $FeCl_2$ ($MnCl_2$ and $CdCl_2$) (10 mg) in an alumina boat was placed in the centre of the tube. The furnace was heated to the growth temperature (580–600 °C for $FePS_3$ and $CdPS_3$ and 590–600 °C for $MnPS_3$). The heating temperature of S (10 mg) is 150 °C and P (10 mg) is 450 °C. The growth time is 3 min. Ar at a flow rate of 80 s.c.c.m. was used as the carrier gas.

$FePSe_3$ ($MnPSe_3$ and $CdPSe_3$). $FeCl_2$ (10 mg) in an alumina boat was placed in the centre of the tube. The furnace was heated to the growth temperature (580–600 °C for $FePSe_3$ and $CdPSe_3$ and 590–600 °C for $MnPSe_3$). The heating temperature of Se is 250 °C and P is 450 °C. The growth time is 3 min. Ar/H_2 at a flow rate of 80/6 s.c.c.m. was used as the carrier gas.

$NiPS_3$ (VPS_3). $NiCl_2$ (VCl_3) (10 mg) in an alumina boat was placed in the centre of the tube. The furnace was heated to the growth temperature (580–600 °C). The heating temperature of S (10 mg) is 150 °C and P (10 mg) is 450 °C. The growth time is 3 min. Ar/H_2 at a flow rate of 80/6 s.c.c.m. was used as the carrier gas.

$CoPS_3$. $CoCl_2$ (10 mg) in an alumina boat was placed in the centre of the tube. The furnace was heated to the growth temperature (670–750 °C). The heating temperature of S (10 mg) is 150 °C and P (10 mg) is 450 °C. The growth time is 3 min. Ar/H_2 at a flow rate of 80/6 s.c.c.m. was used as the carrier gas.

$ZnPS_3$. $ZnCl_2$ (10 mg) in an alumina boat was placed in the centre of the tube. The furnace was heated to the growth temperature (600–700 °C). The heating temperature of S (10 mg) is 150 °C and P (10 mg) is 450 °C. The growth time is 3 min. Ar/H_2 at a flow rate of 80/6 s.c.c.m. was used as the carrier gas.

$Pd_3P_2S_8$. $PdCl_2$ (10 mg) in an alumina boat was placed in the centre of the tube. The furnace was heated to the growth temperature (650–750 °C). The heating temperature of S (10 mg) is 150 °C and P (10 mg) is 450 °C. The growth time is 4 min. Ar/H_2 at a flow rate of 80/6 s.c.c.m. was used as the carrier gas.

PdPSe. $PdCl_2$ (10 mg) in an alumina boat was placed in the centre of the tube. The furnace was heated to the growth temperature (650–750 °C). The heating temperature of Se (10 mg) is 250 °C and P (10 mg) is 450 °C. The growth time is 4 min. Ar/H_2 at a flow rate of 80/6 s.c.c.m. was used as the carrier gas.

$Mn_xCd_{1-x}PS_3$. $MnCl_2$ (5 mg) and $CdCl_2$ (5 mg) in an alumina boat were placed in the centre of the tube. The furnace was heated to the growth temperature (~585–600 °C). The heating temperature of S (10 mg) is 150 °C and P (10 mg) is 450 °C. The growth time is 3 min. Ar at a flow rate of 80 s.c.c.m. was used as the carrier gas.

$Mn_xCd_{1-x}PSe_3$. $MnCl_2$ (5 mg) and $CdCl_2$ (5 mg) in an alumina boat were placed in the centre of the tube. The furnace was heated to the growth temperature (~585–600 °C). The heating temperature of Se (10 mg) is 250 °C and P (10 mg) is 450 °C. The growth time is 3 min. Ar/H_2 at a flow rate of 80/6 s.c.c.m. was used as the carrier gas.

$Mn_xFe_{1-x}PS_3$. $MnCl_2$ (5 mg) and $FeCl_2$ (5 mg) in an alumina boat were placed in the centre of the tube. The furnace was heated to the growth temperature (~590–600 °C). The heating temperature of S (10 mg) is 150 °C and P (10 mg) is 450 °C. The growth time is 3 min. Ar at a flow rate of 80 s.c.c.m. was used as the carrier gas.

$Mn_xFe_{1-x}PSe_3$. $MnCl_2$ (5 mg) and $FeCl_2$ (5 mg) in an lumina boat were placed in the centre of the tube. The furnace was heated to the growth temperature (~590–600 °C). The heating temperature of Se (10 mg) is 250 °C and P (10 mg) is 450 °C. The growth time is 3 min. Ar/H_2 at a flow rate of 80/6 s.c.c.m. was used as the carrier gas.

$Fe_xCd_{1-x}PS_3$. $FeCl_2$ (5 mg) and $CdCl_2$ (5 mg) in an alumina boat were placed in the centre of the tube. The furnace was heated to the growth temperature (~585–600 °C). The heating temperature of S (10 mg) is 150 °C and P (10 mg) is 450 °C. The growth time is 3 min. Ar at a flow rate of 80 s.c.c.m. was used as the carrier gas.

$Fe_xCd_{1-x}PSe_3$. $FeCl_2$ (5 mg) and $CdCl_2$ (5 mg) in an alumina boat were placed in the centre of the tube. The furnace was heated to the growth temperature (~585–600 °C). The heating temperature of Se (10 mg) is 250 °C and P (10 mg) is 450 °C. The growth time is 3 min. Ar/H_2 at a flow rate of 80/6 s.c.c.m. was used as the carrier gas.

$Mn_xFe_yCd_{1-x-y}PS_3$. $MnCl_2$ (3 mg), $FeCl_2$ (3 mg) and $CdCl_2$ (3 mg) in an alumina boat were placed in the centre of the tube. The furnace was heated to the growth temperature (~585–600 °C). The heating temperature of S (10 mg) is 150 °C and P (10 mg) is 450 °C. The growth time is 3 min. Ar at a flow rate of 80 s.c.c.m. was used as the carrier gas.

$Mn_xFe_yCd_{1-x-y}PSe_3$. $MnCl_2$ (3 mg), $FeCl_2$ (3 mg) and $CdCl_2$ (3 mg) in an alumina boat were placed in the centre of the tube. The furnace was heated to the growth temperature (~585–600 °C). The heating temperature of Se (10 mg) is 250 °C and P (10 mg) is 450 °C. The growth time is 3 min. Ar/H_2 at a flow rate of 80/6 s.c.c.m. was used as the carrier gas.

$CuCr(PS_3)_x$. $CuCl_2$ (5 mg) and $CrCl_2$ (5 mg) in an alumina boat were placed in the centre of the tube. The furnace was heated to the growth temperature (~620–650 °C). The heating temperature of S (10 mg) is 150 °C and P (10 mg) is 450 °C. The growth time is 3 min. Ar/H_2 at a flow rate of 80/6 s.c.c.m. was used as the carrier gas.

STEM-ADF imaging. The STEM samples were prepared with a poly(methyl methacrylate) (PMMA)-assisted method or PMMA-free method with the assistance of isopropyl alcohol droplets. For some water-sensitive materials, we used a non-aqueous transfer method. STEM imaging and EELS analysis were performed on a JEOL 2100F instrument with a cold field-emission gun and an aberration corrector (delta corrector) operating at 60 kV. A Gatan GIF Quantum instrument was used for recording the EELS spectra. The inner and outer collection angles for the STEM image (β1 and β2) were 62 and 129–140 mrad, respectively, with a convergence semi-angle of 35 mrad. The beam current was about 15 pA for the annular dark-field imaging and EELS chemical analysis.

TGA-DSC. The TGA and differential scanning calorimetry (DSC) measurements were performed using a NETZSCH STA 449C thermal analyser. Approximately 10 mg of the sample was loaded into an alumina crucible and heated at 50 K min^{-1} from 20 to 700 °C. Ar at a flow rate of 40 ml min^{-1} was used as the carrier gas.

Device fabrication and transport measurements. The Hall bar are patterned on few-layer Fe-based 2D materials using electron-beam lithography. Ti/Au (5/50 nm) electrodes are deposited using the thermal evaporator, followed by the lift-off process. To avoid oxidation, the samples were covered by PMMA in a glove box after growth.

Data availability

The main data supporting the findings of this study are available within the article and Supplementary Information. Additional data are available from the corresponding authors upon reasonable request.

Acknowledgements

This work was supported by the National Key R&D Program of China (grant no. 2020YFA0308800) and the NSF of China (grant nos. 62174013, 11504046 12061131002 and 11734003). This work was also supported by the National Research Foundation—Competitive Research Program (NRF-CRP22-2019-0007, NRF-CRP21-2018-0007 and NRF2020-NRF-ISF004-3520). This work was also supported by the Singapore Ministry of Education Tier 3 Programme 'Geometrical Quantum Materials' (MOE2018-T3-1-002), AcRF Tier 2 (MOE2019-T2-2-105) and AcRF Tier 1 RG161/19 and RG7/21. W.B.G. acknowledges the support of NRF CRP by NRF-CRP22-2019-0004. G.L. and L. Lu acknowledge fundings from the National Natural Science Foundation of China under grant numbers 92065203 and 11874406, and the Strategic Priority Research Program of the Chinese Academy of Sciences (grant no. XDB33010300). Y.Y. was supported by the National Key R&D Program of China (grant no. 2016YFA0300600). C.Z. acknowledges the Fundamental Research Funds for the central Universities. F.D. and J.D. acknowledge funding from the Institute for Basic Science, Republic of Korea (IBS-R019-D1) and the use of the IBS-CMCM high-performance computing system Cimulator. This work was also supported by the Innovation Program of Shanghai Municipal Education Commission (no. 2019-01-07-00-09-E00020) and Shanghai Municipal Science and Technology Commission (18JC1412800). Y.-C.L. and K.S. acknowledge JSPS-KAKENHI (JP16H06333 and 18K14119), JSPS A3 Foresight Program and Kazato Research Encouragement Prize. H. Yang acknowledges funding from the Chinese Academy of Sciences (grant nos. XDB33030100). Y.Y. acknowledges the Strategic Priority Research Program of the Chinese Academy of Sciences (grant no. XDB30000000).

Author contributions

J.Z. and Y. Zhou observed the growth mechanism and grew all the materials. J.Z. carried out the Raman and AFM characterizations. C.Z. performed the STEM characterizations and data analysis of the Fe-based samples other than Fe_3GeTe_2. Y.-C.L. and K.S. analysed Fe_3GeTe_2 and all the metal phosphorous chalcogenides. J.Z., Y. Zhou, C. Z. and Z.L. analysed the growth mechanism. Y. Zhou, J.Z. and B.T. performed the X-ray photoelectron spectroscopy test. Y. Zhou, H. Yu and Y.G. performed the TGA-DSC measurements. G.L., R.Z. and Y.Y. performed the electronic structure calculations. J.D. and F.D. performed the DFT calculations on the formation mechanism of FeS_x with different compositions and phases. P.L. and G.L. measured the superconductivity in FeX and ferromagnetism in FeS_2. J.S. measured the SHG properties in MPX_3. Z.W. and W.H. used the infrared photodetector for $FeTe_2$. J.Z., Y. Zhou, C.Z., G.-B.L., Y.Y. and Z.L. wrote the paper. All the authors discussed and commented on the manuscript.

Competing interests

The authors declare no competing interests.

Additional information

Supplementary information The online version contains supplementary material available at https://doi.org/10.1038/s41563-022-01291-5.

Correspondence and requests for materials should be addressed to Jiadong Zhou, Yeliang Wang, Yugui Yao or Zheng Liu.

Peer review information *Nature Materials* thanks Sufei Shi and the other, anonymous, reviewer(s) for their contribution to the peer review of this work.